

Reduction of optical crosstalk in SiPMs due to coupled light guides and investigation of other properties demonstrated with the SensL MicroFJ-60035-TSV

F. Rehbein,^{a,1} T. Bretz,^{a,1} R. Alfaro,^b J. Audehm,^a A. Biland,^{c,1} G. Do,^a M. M. González,^d Y. F. Pérez-Araujo,^d M. Schaufel,^e J. Serna-Franco,^b I. Torres^f

^aPhysics Institute 3A, RWTH Aachen University, Sommerfeldstraße 16, 52074 Aachen, Germany.

^bInstituto de Física, Universidad Nacional Autónoma de México, Ciudad de México, Mexico.

^cETH Zurich, Inst. for Particle Physics and Astrophysics, Otto-Stern-Weg 5, 8093 Zurich, Switzerland.

^dInstituto de Astronomía, Universidad Nacional Autónoma de México, Ciudad de México, Mexico.

^ePhysics Institute 3B, RWTH Aachen University, Sommerfeldstraße 16, 52074 Aachen, Germany.

^fInstituto Nacional de Astrofísica, Óptica y Electrónica, Puebla, Mexico.

E-mail: florian.rehbein@rwth-aachen.de

ABSTRACT: During the past decade, semi-conductor photo sensors have replaced photo multiplier tubes in numerous applications featuring single-photon resolution, insensitivity to magnetic fields, higher robustness and enhanced photo detection efficiency at lower operation voltage and lower costs. This paper presents a measurement of gain, optical crosstalk and dark count rate of 127 Silicon Photo Multipliers (SiPMs) of type SensL MicroFJ-60035-TSV at nominal bias voltage. In SiPMs, optical crosstalk can fake higher multiplicities for single-photon hits. This paper demonstrates that optically coupled light guides reduce this probability significantly. The measured sensors offer a comparably small variation of their breakdown voltage with temperature of only 21.5 mV/K. The manufacturer specifies a limited range of only ± 250 mV for their nominal breakdown voltage. This should allow for operation with small systematic errors without major efforts on temperature-based bias voltage compensation and without calibration of their individual breakdown voltages. This paper proves that the gain distribution of the measured sensors is consistent with the data sheet values.

KEYWORDS: Photon detectors for UV, visible and IR photons (solid-state), Gamma telescopes

¹Corresponding author.

Contents

1	Introduction	1
2	Hardware	3
3	Method	4
4	Results	8
5	Conclusions	9

1 Introduction

In many applications, the ability to detect very faint light flashes requires photo sensors with a high photo detection efficiency and a high level of robustness. Silicon Photo Multipliers (SiPMs) provide durability, low operation voltage, and robustness against bright light exposure. For instance, in imaging air-Cherenkov astronomy, SiPMs were initially applied in the First G-APD Cherenkov Telescope (FACT [1]) as a replacement for classical photo multiplier tubes. The telescope is successfully operated now for almost ten years [2]. Its ability to operate even under bright background illumination, such as moonlight [3], provides an increased duty cycle [2] of almost 30%. The robustness and stability of the sensors allow for consistent unbiased monitoring of astronomical sources enabling unprecedented long-term studies (e. g. [4]).

Significant improvement of the photo detection efficiency of SiPMs during the recent decades have facilitated the construction of compact telescopes with an aperture diameter of only 50 cm [5]. They are also the first imaging air-Cherenkov telescopes utilizing refractive optics based on a Fresnel lens in operation. Based on this design, similar telescopes were constructed to achieve hybrid measurements together with extensive air shower arrays. Hybrid measurements allow resolving the ambiguity on shower age, intrinsic to air shower arrays, and on shower distance, intrinsic to telescopes, enabling for inexpensive low-resolution optics. Measurements are on-going with the IceAct telescope at the IceCube neutrino observatory at the South Pole, for example, for the improvement of veto capabilities [6], and together with the High Altitude-Water Cherenkov Observatory (HAWC [7]) in Mexico for calibration and increased sensitivity [8]. Compared with the original design, these telescopes implement further improvements including solid light guides with an increased collection efficiency and SiPMs with further enhanced photo detection efficiency. This study discusses results obtained with two telescopes at the HAWC site: named the HAWC's Eye telescopes.

Silicon photo multipliers combine multiple Geiger-mode avalanche photo diodes (G-APD) into one sensor. Geiger-mode avalanche photo diodes are also commonly known as single-photon

avalanche diodes (SPAD). A more detailed description of SiPMs is given in [9]. The diodes are operated in Geiger-mode, i. e. above a characteristic voltage, the so-called breakdown voltage. Above this threshold, impinging photons can trigger electron-hole pairs inducing a self-sustaining particle cascade. The initiated current causes a voltage drop at the built-in quenching resistor. When the applied voltage falls below the breakdown voltage, the avalanche is stopped. The released charge is independent of the number of initial electron-hole pairs and depends only on physical properties of the diode and the difference between the applied bias voltage and the breakdown voltage. The charge released by one discharge is commonly referred to as photon equivalent (p. e.). The voltage difference is known as overvoltage. The released charge is also independent of the energy and angle of the incident photon. Random discharges triggered by thermal excitation are known as dark counts.

The arrangement of hundreds to tens of thousands of G-APD cells in one sensor introduces additional noise features into the measured signal, such as optical crosstalk and afterpulses. The probability of afterpulses drops exponentially after the initial breakdown with a decay time comparable to the recharge time of the cell. Their released charge is intrinsically limited by the maximum charge the cell so that contributions from afterpulses are highly suppressed during the early recharge phase. In the present study, the effect of afterpulses is neglected because the analysis is based on charge integration over only a small time window and the total afterpulse probability of recent sensors is less than a few percent¹.

Optical crosstalk is induced by photons emitted during recombination triggering secondary breakdowns in neighboring cells. The crosstalk probability is defined as the fraction of signals containing at least one secondary breakdown. A detailed description of different photon paths relevant to the crosstalk process is given in [11]. A measurement of spatially resolved optical crosstalk is presented in [12]. Crosstalk is mainly a challenge in cases in which a low number of photons should be measured accurately. However, for high multiplicities, crosstalk just contributes to a statistical increase of the signal. Usually, a low crosstalk probability can only be achieved by a selection of devices specifically built with such characteristics. Modern SiPMs comprise thin optical trenches that surround the active area of the cells to reduce direct crosstalk between neighbouring cells [13]. This makes the photons reflected at the protective window the dominant contribution to the remaining crosstalk.

This study demonstrates that a well-designed light guide that is optically coupled to the protective window decreases crosstalk probability. If a transparent material with a comparable refractive index is coupled to the protective window, total reflection is suppressed. The special shape of a light guide directs the transmitted photons out of its entrance aperture, thus avoiding triggers in neighboring cells.

¹< 5 % for SensL MicroFJ-60030-TSV at 5 V overvoltage [10]

2 Hardware

The cameras of the two HAWC's Eye telescopes feature 64 sensors each. Out of those, 61 sensors are optically coupled to solid light guides to increase their light collection area. The remaining three SiPMs ("blind pixels") are used for calibration. Due to transport damage, one of the two cameras misses one sensor and three light guides. Moreover, one of its light guides remains loosely on the respective SiPM.

Sensors and Bias Power Supply

The utilized sensors are of type SensL² MicroFJ-60035-TSV [10] which are operated at an overvoltage of 5 V. Each sensor has an active area of $6.07 \times 6.07 \text{ mm}^2$ and consists of 22 292 G-APD cells. The sensors achieve a peak photo detection efficiency of 50 % at a wavelength of 420 nm if operated at 6 V overvoltage above their nominal breakdown voltage of 24.5 V. The data sheet defines the minimum and maximum breakdown voltage as 24.2 V and 24.7 V at a temperature of 21 °C. This range corresponds to a maximum gain variation of $\pm 5 \%$ at 5 V overvoltage. It is expected that the typical sensor-to-sensor variation of breakdown voltages is smaller. The bias voltage is supplied from a power supply based on the design discussed in [14]. It adjusts the applied voltage of each sensor individually to compensate for a change of overvoltage with the change of breakdown voltage with temperature. The temperature sensors provide an absolute precision of 1 K without additional calibration. In total, 64 temperature sensors are located on the backside of the printed circuit board hosting the SiPMs. It can be expected that their temperature matches the SiPM's internal temperature with a deviation of not more than 1 K. In total, this system provides a precision of the temperature measurement better than 2 K corresponding to a systematic relative deviation in overvoltage of less than 1 % for the given temperature coefficient of 21.5 mV/K. After calibration and without load, each channel of the bias power supply provides a voltage with a precision of typically 2 mV, but not higher than 10 mV. Compared to the overvoltage, the precision of the power supply can therefore be neglected. This yields a total systematic relative uncertainty of the gain of 5 %. The dark count rate is specified to be less than 100 kHz/mm². Generally, dark counts allow for determining sensor properties such as the crosstalk probability and the gain. This helps to characterize and calibrate the SiPMs.

Light Guides

Light guides are often used in SiPM applications to increase their small photosensitive area. They are particularly common in SiPM cameras to decrease dead space at reduced total costs. In the camera of the FACT telescopes, solid light guides are successfully applied since 2011 [1, 15].

The required acceptance angle of the applied light guides is usually defined by the numerical aperture of the imaging optics and by the requirements on the attenuation of stray light. Their exit aperture is given by the SiPM surface area. These constraints and the acceptance angle of the SiPM inherently limit their maximum concentration factor, since according to Liouville's theorem, the phase-space distribution function is constant along the trajectories of the system. As the refractive

²now OnSemi

index of the material changes the effective path length of the trajectories, the maximum concentration factor is proportional to the refractive index n squared, i. e.

$$\frac{A}{a} \propto n^2 \quad (2.1)$$

with the entrance aperture A and the exit aperture a . The acceptance angle of the sensor is always limited by the critical angle for total reflection at the silicon surface.

The light guides of the HAWC's Eye camera are made of Plexiglas with a refractive index which is comparable to the one of the protective window of the sensors. The refractive index of the Plexiglas at 436 nm is 1.50 [16] and for the sensor 1.53 [10]. Each light guide is optically coupled to its sensor with a very thin layer of optical glue, also of similar refractive index. Their shape was designed to support an opening angle of 33.7° corresponding to the view of an edge pixel at 60 mm distance from the camera center and a numerical aperture $f/D = 502 \text{ mm} / 550 \text{ mm} = 0.9$ of the optical system [17]. This leads to a compression factor of 5.5. With their refractive index of $n \approx 1.5$, they achieve a concentration factor about as twice as large when compared to a corresponding hollow light guide, see also a more detailed discussion in [18].

If the overall performance of solid and hollow light guides is evaluated for the case of an optimized concentration factor, also reflection and absorption have to be considered: Total reflection outperforms coated or polished surfaces. Internal absorption for Plexiglas is in the order of 1 %/cm and can be neglected³. If light guides are covered by a protective window which is optically not coupled, an additional Fresnel loss of about 4 % has to be taken into account at each window-air interface. This is always the case in the application of hollow light guides.

Optimized light guides are designed such that the maximum acceptance angle of the silicon is exhausted by incoming rays. That means that for each outgoing ray, at least one light path exists that leads the photon out of the guide. Consequently, optical coupling to a light guide leads to a reduced probability for these photons to be reflected back into the sensor. Contrary, in case of the application of non-optimized guides, photons might be internally reflected back to the sensor and trigger random cells. As direct neighbors might be discharged already by other crosstalk photons, random cells have a higher probability for being charged and therefore to trigger. Although this does generally not increase crosstalk probability as it is dominated by the probability to create the first additional crosstalk trigger, it can result in a relative increase of higher multiplicities.

3 Method

A dark count spectrum is a histogram measuring charge induced from thermal excitation. Therefore, one records randomly triggered events without ambient light to minimize the background of impinging photons. Analysing dark count spectra of the photo sensors allows to determine their characteristics such as gain, crosstalk probability, and recharge time scale of the sensors.

For each telescope, 100 000 events were triggered at a frequency of 80 Hz limited only by the maximum trigger rate of the data acquisition system. The spatial temperature average of the sensors

³Note that absorption in data sheets usually includes the effect of Fresnel reflection at both surfaces.

of both focal planes was $28\text{ }^{\circ}\text{C}$ with a typical spread of less than $1\text{ }^{\circ}\text{C}$. All individual sensors were stable during data taking within $0.2\text{ }^{\circ}\text{C}$. The channels are read out with the maximum sampling depth of 1024 samples per channel at a sampling rate of 2 Gsample/s. An example of a signal trace is shown in Figure 1.

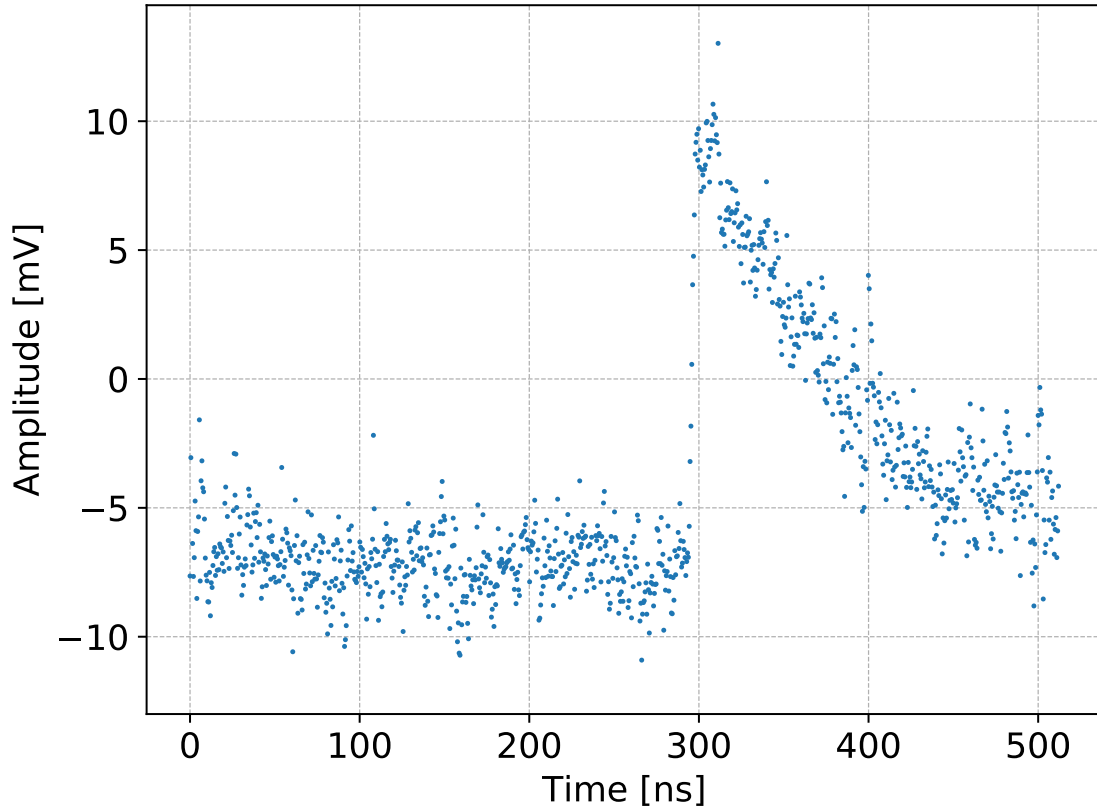


Figure 1: Example of a signal trace. The sampling rate corresponds to 2 Gsample/s.

A similar study on dark count spectra has been published by FACT [19], which uses the same data acquisition system and software as described in [1]. Therefore, the same algorithm to extract the pulses from the recorded data was adopted. As it is explained in detail there, the approach is described here only briefly for completeness.

In the first stage, a baseline is determined and subtracted for each channel individually. As some channels suffer from periodic electronic noise, a sliding average with an adapted length of 10 samples is applied. The resulting trace is scanned for a threshold crossing of 5 mV between two consecutive samples. Then, a local maximum is searched between 5 and 35 samples after the threshold crossing. The arrival time is defined by the last sample within the 30 samples before the local maximum with an amplitude that does not fall 50% of the maximum value. Integrating the raw signal over 30 samples after the arrival time yields the extracted signal.

Since the signals of three pixels in each camera are additionally split to provide an additional calibration output, their measured signal is attenuated by 18% compared to the other 61 pixels.

Spectrum Function

The properties of the sensors are extracted from their dark count spectrum. To properly describe the measured dark count spectrum, one has to account for the probability P_N to measure a multiplicity of N breakdowns induced by the initial breakdown of a single cell as well as noise that smears out this distribution. In [19] various distribution functions are compared. It is demonstrated that the best description of the dark count spectra is the modified Erlang distribution with coefficients given by

$$P_N = \frac{(Nq)^{N-1}}{[(N-1)!]^\nu} \quad \text{with} \quad q \equiv p \cdot e^{-p}. \quad (3.1)$$

The fit parameter ν originates from the fact that the number of potential crosstalk triggers by each breakdown is limited by the geometry of the sensor and is usually $\nu \sim 1$. The parameter p describes the probability for a breakdown to trigger an additional breakdown in a neighbouring cell and should not be confused with what is generally referred to as crosstalk probability. The crosstalk probability can be derived as

$$p_{xt} = \frac{\sum_{n=2}^{\infty} P_n}{\sum_{n=1}^{\infty} P_n}. \quad (3.2)$$

Two types of noise sources are considered in this analysis. The charge released in each avalanche undergoes cell-to-cell fluctuations and thus scales with the number of breakdowns. The electronics noise is independent of the multiplicity. Both types of noise are assumed to be Gaussian. Therefore, the measured dark count spectrum can be described by a sum of Gaussian distributions for multiplicity N with width given by,

$$\sigma_N = \sqrt{\sigma_{el}^2 + N\sigma_{pe}^2} \quad (3.3)$$

where σ_{el} and σ_{pe} are the Gaussian widths for the electronics noise and the amplitude dependent charge fluctuations respectively. Introducing the gain g and a baseline shift x_0 , the position of the mean of each Gaussian and their normalization are defined as

$$x_n = x_0 + n \cdot g \quad \text{and} \quad a_n = \sigma_n \sqrt{2\pi}. \quad (3.4)$$

The resulting distribution can be written as

$$f(x) = A_1 a_1 \cdot \sum_{n=1}^{n=\infty} P_n \frac{e^{-\frac{1}{2}[\frac{x-x_n}{\sigma_n}]^2}}{a_n}. \quad (3.5)$$

The parameter A_1 denotes the amplitude of the single-p.e. peak. Integration of $f(x)$ over the whole range of extracted signals results in the total number of dark counts and can be used to calculate the dark count rate.

For each SiPM, the extracted signals are filled into a histogram. The histogram is then fitted with a log-likelihood method with the distribution described in Equation 3.5. The resulting offset

and gain are then used to normalize the signals to their multiplicity N . The offset is generally in the order of a few percent of the gain and therefore negligible. The 111 SiPMs which are optically coupled to a light guide and do not suffer a reduced gain are expected to have comparable noise features. After gain normalization, they are compiled into a single histogram.

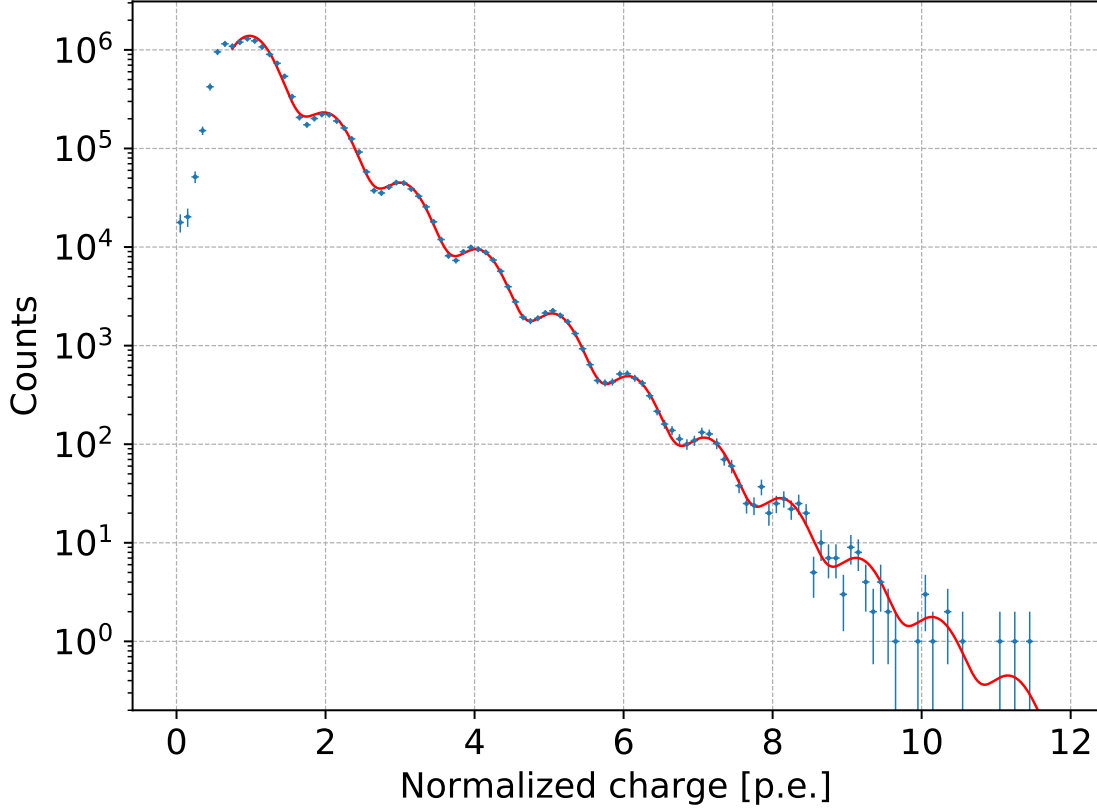


Figure 2: Normalized dark count spectrum compiled from the majority of all SiPMs that are expected to have identical properties, i. e. which are optically coupled to a light guide and do not suffer a reduced gain. The red line shows the fit as introduced in Equation 3.5. For a dark count rate of roughly 53 kHz/mm^2 , as discussed in Section 4, a multiplicity of 10 yields a rate of only 0.5 Hz/mm^2 corresponding to a suppression of six orders of magnitude.

The resulting histogram is displayed in Figure 2. By fitting the distribution function described in Equation 3.5, the exponent ν (see Equation 3.1) is estimated to 0.920 ± 0.003 . Since its value affects the fit mainly at high multiplicities and is intrinsic to the type of SiPM in use, the higher multiplicities accessible in the combined spectrum allow for a more precise determination of the exponent ν . It is fixed in the subsequent fits to the individual SiPM spectra.

An example of a fit to the spectrum of two single SiPMs is shown in Figure 3. The fit is used to determine properties of each pixel individually, including the dark count rate, gain, and crosstalk probability.

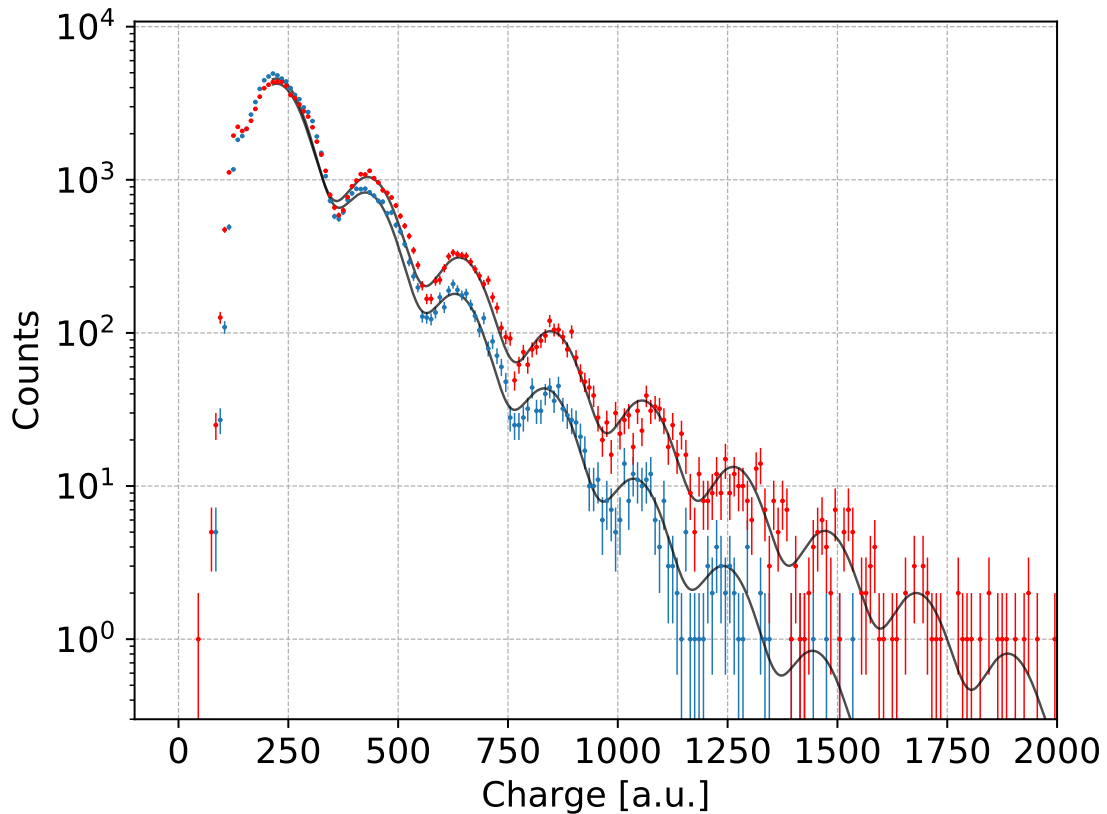


Figure 3: Dark count spectrum extracted from a single SiPM optically coupled to a light guide (blue) and a blind pixel without a light guide (red). The grey lines show the fit to the distribution as introduced in Equation 3.5 with the exponent ν fixed to the value extracted from the compiled spectrum shown in Figure 2.

4 Results

Gain Distribution. Figure 4 shows the distribution of the gain normalized to the average gain of all 127 pixels. The distribution has a variance of roughly 3%. All values are within a range from 92% to 107%. As the breakdown voltage has not been calibrated individually for each sensor, the width of the distribution is well consistent with systematic deviations coming from the provided operation range of the manufacturer ($\pm 5\%$) and the precision of the temperature feedback system ($\pm 1\%$).

Optical Crosstalk. The distribution of the crosstalk probability as evaluated by fitting the modified Erlang distribution to the measured dark count spectra is depicted in Figure 5. Two distinct classes of SiPMs corresponding to the SiPMs with and without an optically coupled light guide are visible. The ten SiPMs without optically coupled light guides have a larger crosstalk probability as discussed in section 2.

Dark Count Rate. The measured dark count rate is consistent for 114 sensors with a log-normal distribution with a mean of $52.7^{+3.0}_{-2.8}$ kHz/mm². Three sensors show a dark count rate higher by a factor two. Two of these sensors are located at identical places in their corresponding camera. This might point to a light leak through nearby screw holes into the lens tube originating from LEDs of the readout electronics. The location of the third sensor coincides with the missing sensor in the other. For the applied overvoltage of 5 V, the data sheet values for the dark count rate correspond to about 75 kHz/mm² at 21 °C. The lower measured value is most likely an effect of the applied method. The comparably long decay times of the pulse of about 80 ns defined by the SiPM's recovery time and the electronics, naturally lead to an inefficient pulse detection at the edges of the readout window. This effect, which is not accounted for in this analysis, eventually reduces the effective measurement time and therefore the measured dark count rate. Excellent quality of SiPM production can also not be excluded as a reason, as other laboratory measurements of these sensors have also shown results at the lower edge of the data sheet values.

5 Conclusions

In this study, the characteristics of 127 SiPM sensors of type SensL MicroFJ-60030-TSV have been evaluated. This has been done using the cameras of two HAWC's Eye telescopes applying readout electronics originally produced for the FACT telescope. Out of these 127 sensors, 117 sensors are properly coupled to solid optical light guides. The bias power has been provided by a power supply achieving a precision of $\ll 1\%$ that was neglected in this study. The temperature-based overvoltage stabilization works with a precision corresponding to 1 % of the sensors overvoltage including systematic effects from uncalibrated temperature sensors. For temperature-based voltage compensation, the temperature coefficient from the data sheet was applied. The maximum range of allowed breakdown voltages given by the manufacturer corresponds to $\pm 5\%$ for an overvoltage of 5 V. Therefore, the systematic contributions are dominated by the knowledge of the breakdown voltage.

The measurement of the gain of all 127 sensors showed a maximum deviation from the mean value of $\pm 7.5\%$ with a variance of only 3 %. This is well consistent with the data sheet of the manufacturer. While in a similar study of the FACT camera, the breakdown voltage for each sensor had still to be calibrated to achieve a variance of 2.4 %, this study intentionally has omitted all calibrations related to the SiPMs themselves and applied an uncalibrated temperature-based voltage compensation circuit.

In addition, the crosstalk probability of 117 sensors with, and nine without, optical coupling to light guides has been investigated. Since with optically coupled light guides, crosstalk photons that are reflected on the protective window can leave the SiPM, the probability for optical crosstalk has decreased. A reduction by 31 % from an average probability of 26 % for the bare sensors to an average probability of 18 % has been confirmed for sensors with an optically coupled light guide. An additional single light guide shows an unclear status of optical coupling. As its crosstalk value falls exactly into the distribution of the nine pixels without light-guide, it can be concluded that no

proper coupling exists for this sensor as well.

Reduction of crosstalk probability was also investigated in a laboratory setup for the solid light guides used in the FACT telescope while they were coupled to SiPMs of type Hamamatsu S14520-3050 VN. A relative decrease of the optical crosstalk probability by about 29 % [20] was observed. This result confirms the significant reduction demonstrated in this paper. As a different sensor type and light guides of different geometrical properties were applied, the measured values can not be compared directly.

The analysis of the performance of the photo sensors installed in the two HAWC's Eye telescopes confirms the high precision of recent SiPMs. It demonstrates that even for high precision requirements, the application of data sheet values is sufficient. Apart from a reasonable precise power supply, no additional calibration is necessary. This study also confirms that coupling the sensors to well-designed light guides reduces optical crosstalk between neighboring cells significantly.

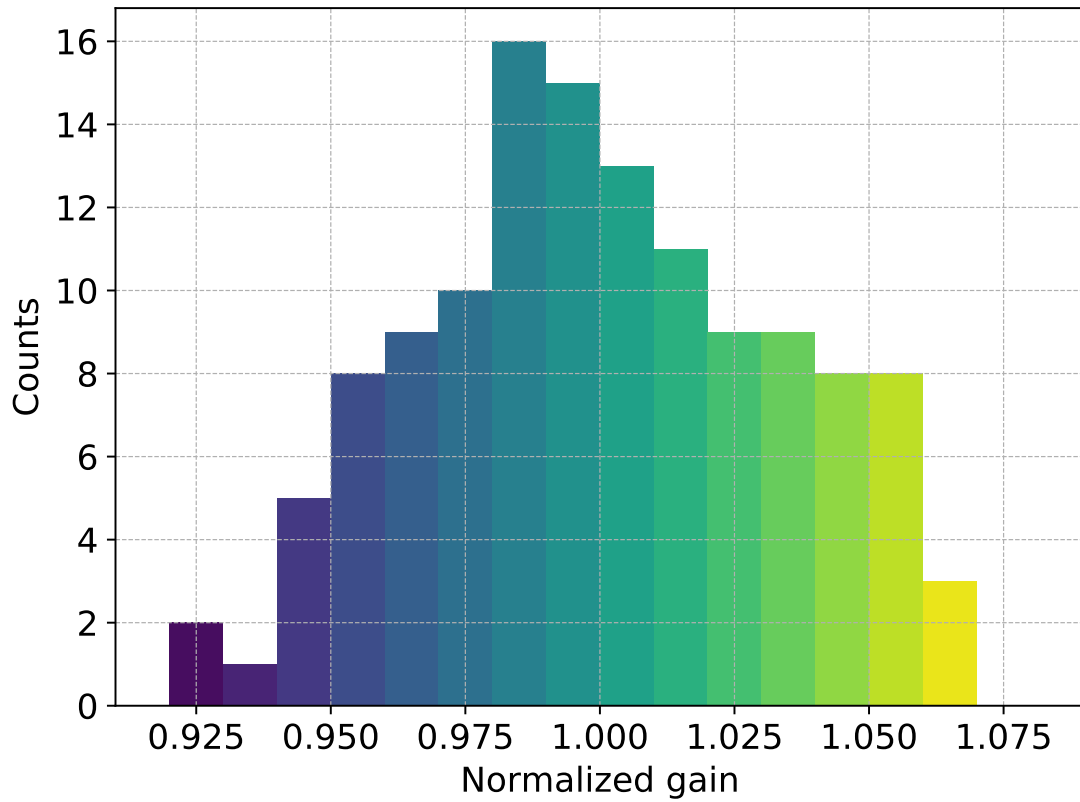
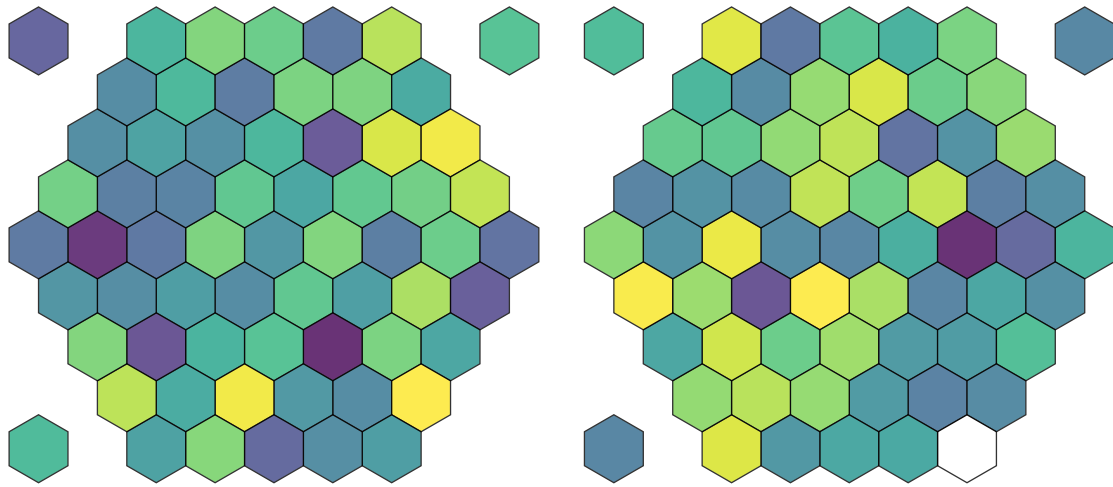


Figure 4: Distribution of the resulting gain from a fit to the dark count spectrum of each of the 127 SiPMs normalized to the average gain. The gain of the six pixels with a lower electronics gain has been scaled accordingly. The arrangement in the two cameras shows a homogeneous distribution. The colors of the histogram bars match the colors of the camera display. The color scale ranges from purple (low) to yellow (high).

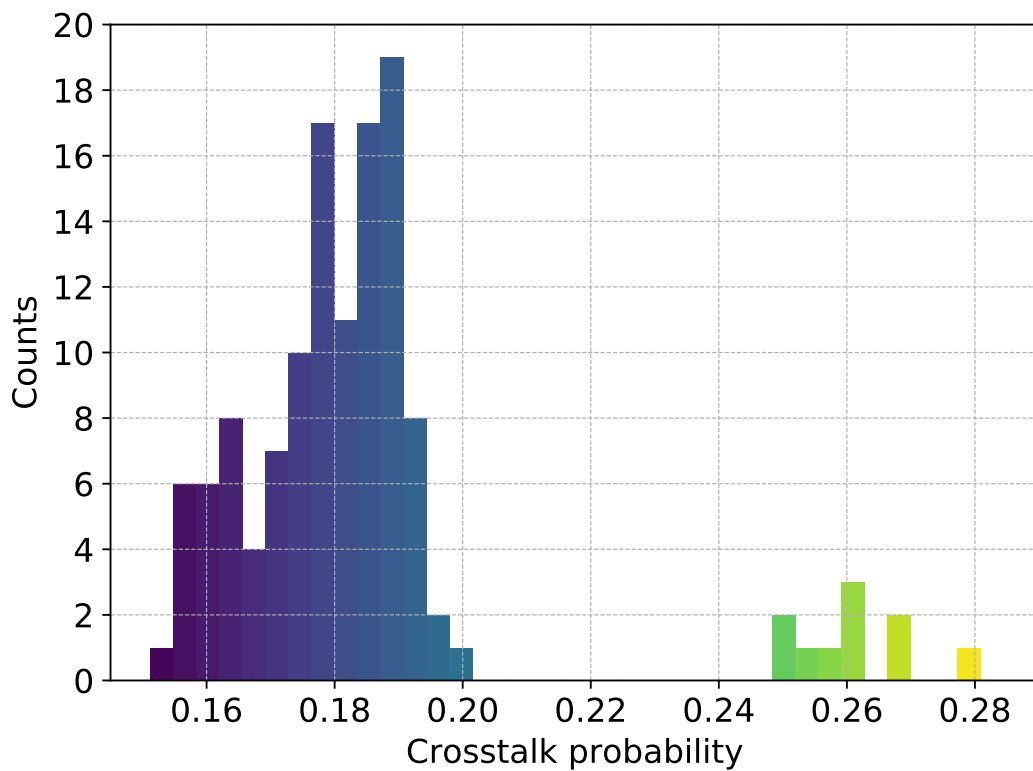
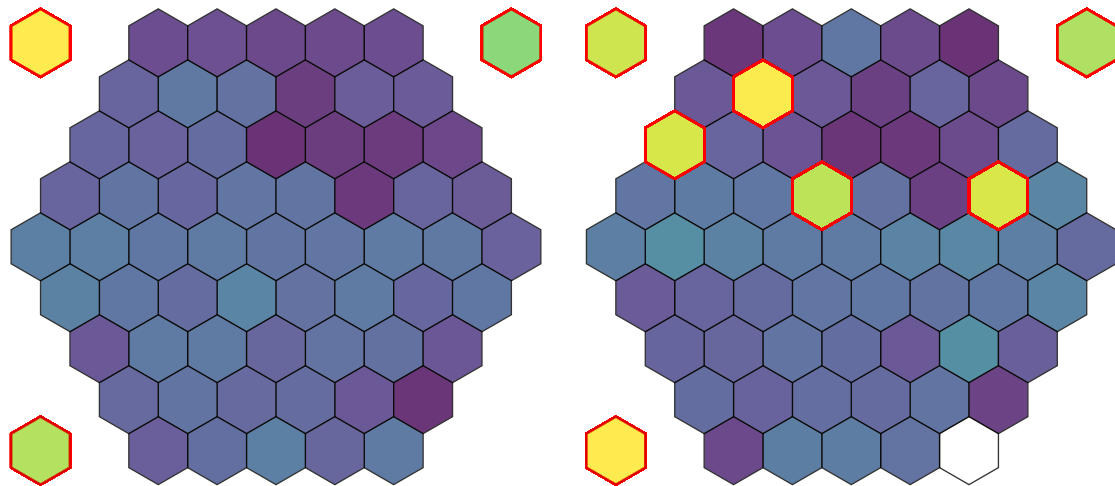


Figure 5: Distribution of the resulting crosstalk probability from a fit to the dark count spectrum of each of the 127 SiPMs. Two separated distribution are visible. The locations of the corresponding pixels in the two cameras coincide exactly with the pixels with and without an optically coupled light guide. Pixels without coupling are marked in red. The colors of the histogram bars match the colors of the camera display. The color scale ranges from purple (low) to yellow (high).

Acknowledgments

We thank Johannes Schumacher for his excellent design of the bias power supply, and the electronics and mechanics workshop of the Physics Institute 3A and 3B of RWTH Aachen University for their support. We also acknowledge Kazuhiro Furuta, Akira Okumura, and Hiroyasu Tajima for their measurement cited in the conclusions. This work was partially funded by the Excellence Initiative of the German federal and state governments and the German Academic Exchange Service, the DGAPA PAPIIT (project number IG101320) and the CONACYT-DAAD (project 279446).

References

- [1] H. Anderhub et al. (FACT Collaboration), *Design and operation of FACT - the first G-APD Cherenkov telescope*, *JINST* **8** (2013) P06008.
- [2] D. Dorner et al. (FACT Collaboration), *FACT - Highlights from more than Seven Years of Unbiased Monitoring at TeV Energies*, In *Proceedings of the 36th ICRC*, *PoS (ICRC 2019)* 665.
- [3] M. L. Knoetig et al. (FACT Collaboration), *FACT - Long-term stability and observations during strong Moon light*, In *Proceedings of the 33rd ICRC 2013*, [arXiv:1307.6116](https://arxiv.org/abs/1307.6116).
- [4] M. Beck et al. (FACT Collaboration), *FACT - Probing the Periodicity of Mrk 421 and Mrk 501*, In *Proceedings of the 36th ICRC*, *PoS (ICRC 2019)* 630.
- [5] T. Bretz et al., *A compact and light-weight refractive telescope for the observation of extensive air showers*, *JINST* **13** (2018) P07024.
- [6] D. Rysewyk et al., *Atmospheric Cherenkov Telescopes as a Potential Veto Array for Neutrino Astronomy*, *Astroparticle Physics* **117** (2020) 102417.
- [7] M. A. Mostafá et al. (HAWC Collaboration), *The High Altitude Water Cherenkov Observatory*, *Nuclear and Particle Physics Proceedings* **279-281** (2016) 87-94.
- [8] J. Audehm et al. (HAWC Collaboration), *HAWC's Eye - Implementing hybrid detection at the HAWC Gamma-Ray Observatory*, In *Proceedings of the 36th ICRC*, *PoS (ICRC 2019)* 636.
- [9] E. Garutti, *Silicon photomultipliers for high energy physics detectors*, *JINST* **6** (2011) C10003.
- [10] ON Semiconductor, *Data sheet J-Series SiPM Sensors*, *Datasheet Rev. 6* (2018). Accessed: 2020-02-10.
- [11] I. Rech et al., *Optical Crosstalk in Single Photon Avalanche Diode Arrays: A New Complete Model*, *Optics Express* **16** (2008) 8381-8394.
- [12] E. Engelmann, E. Popova and S. Vinogradov, *Spatially Resolved Dark Count Rate of SiPMs*, *The European Physical Journal C* **78** (2018) 971.
- [13] R. Pagano et al., *Optimized silicon photomultipliers with optical trenches*, In *Proceedings of the 41st ESSDERC* (2011) 183-186, DOI: [10.1109/ESSDERC.2011.6044204](https://doi.org/10.1109/ESSDERC.2011.6044204).
- [14] M. Schaufel et al. (HAWC Collaboration), *Small size air-Cherenkov telescopes for ground detection arrays - a possible future extension?*, In *Proceedings of the 35th ICRC*, *PoS (ICRC 2017)* 786.
- [15] B. Huber et al. (FACT Collaboration), *Solid light concentrators for small-sized photosensors used in Cherenkov telescopes*, In *Proceedings of the 32nd ICRC* **9** (2011) 2-5.
- [16] G. Beadie et al., *Refractive index measurements of poly(methyl methacrylate) (PMMA) from 0.4-1.6 μm* , *Applied Optics* **54** (2015) F139-F143.

- [17] J. P. Koschinsky, *Development of a 61-Pixel Camera for the IceAct Imaging Air Cherenkov Telescope*, Master's thesis, RWTH Aachen University, 2017.
- [18] T. Bretz and M. Ribordy, *Design constraints on Cherenkov telescopes with Davies-Cotton reflectors*, *Astroparticle Physics* **45** (2013) 44-45.
- [19] A. Biland et al. (FACT Collaboration), *Calibration and performance of the photon sensor response of FACT - the first G-APD Cherenkov telescope*, *JINST* **9** (2014) P10012.
- [20] H. Tajima, Private Communication, 2020.